Using a synoptic-scale mixing diagnostic to explain global precipitation variability from weekly to interannual time scales

Article

Published Version

It is advisable to refer to the publisher's version if you intend to cite from the work. See Guidance on citing.

www.reading.ac.uk/centaur

CentAUR

Central Archive at the University of Reading

Reading's research outputs online

Using a Synoptic-Scale Mixing Diagnostic to Explain Global Precipitation Variability from Weekly to Interannual Time Scales

Gabriel M. P. Perez,[a] Pier Luigi Vidale,[a,b] Helen Dacre,[a] and Jorge L. García-Franco[c]

[a] *Department of Meteorology, University of Reading, Reading, United Kingdom*
[b] *National Centre for Atmospheric Science, Reading, United Kingdom*
[c] *Department of Physics, University of Oxford, Oxford, United Kingdom*

ABSTRACT: Precipitation often happens along organized filaments or bands of moisture such as convergence zones. Recent regional studies have shown that these moisture filaments arise from synoptic-scale mixing features known as attracting Lagrangian coherent structures (LCSs). In this study, we present a climatology of synoptic-scale mixing and investigate its covariability with precipitation on temporal scales ranging from weekly to interannual. We characterize mixing with the finite-time Lyapunov exponent (FTLE), a measure of parcel deformation, in ERA5 data between 1980 and 2009. Attracting LCSs are identified as ridges of the FTLE. At the interannual time scale, we compare El Niño and La Niña events and find that composites of precipitation and mixing anomalies share similar spatial patterns. We also compare summer and winter seasons and find that composites of seasonal-mean precipitation and mixing anomalies present similar characteristics, with precipitation being particularly intense (weak) where mixing is strong (weak). In particular, these patterns closely match the typical signatures of the intertropical convergence zone (ITCZ) and monsoon systems and the migrations of extratropical cyclone tracks. At the subseasonal scale, we employ daily composites to investigate the influence of the Madden–Julian oscillation and the North Atlantic Oscillation on the mixing regimes of the Atlantic and east Pacific; our results indicate that these oscillations control the synoptic-scale horizontal mixing and the occurrence of LCSs as to suppress or enhance precipitating systems like the ITCZ and the South Atlantic convergence zone. The results presented in this first climatology of synoptic-scale mixing and LCSs indicate that these are powerful diagnostics to identify circulation mechanisms underlying precipitation variability.

KEYWORDS: Intertropical convergence zone; South Atlantic convergence zone; South Pacific convergence zone; Lagrangian circulation/transport; Climatology; Kinematics

1. Introduction

Water vapor in Earth's atmosphere is constantly sourced from the surface by evaporation and removed by precipitation. Notable moisture sources are on the sea surface under subtropical anticyclones, while important sinks can be found along the intertropical convergence zone (ITCZ) and over tropical and subtropical landmasses under the action of convergence zones and monsoon systems (Wills and Schneider 2015). The median lifetime of water vapor in the atmosphere is approximately 4 days (Läderach and Sodemann 2016). During their lifetime, moist parcels are deformed by the large-scale flow such that filaments and bands of high moisture concentration arise. These moist bands are often associated with weather events such as convergence zones (Kodama 1992) and atmospheric rivers (Dacre et al. 2015).

The ceaseless process of reshaping the horizontal moisture distribution is Lagrangian in essence, as it depends on the history of air masses during the residence time of water vapor. Although Eulerian horizontal velocity fields can be used to quantify instantaneous or time-averaged convergence (Herdies et al. 2002; Berry and Reeder 2014), they cannot reveal the kinematical structures organizing the moisture transport. This is because, in the time-dependent atmospheric flow, streamlines and pathlines quickly diverge. Therefore, frameworks that incorporate the Lagrangian nature of mixing are more appropriate to investigate kinematical structures of accumulation of moisture and other tracers whose residence times are comparable or longer than the dominant time scales of motion (Huntley et al. 2015; Garaboa-Paz et al. 2017; Perez et al. 2021).

The nature of mixing in a flow can be characterized by the stretching and folding of its fluid parcels (Ottino 1989), a process that determines how tracers and properties are redistributed by advection (Pierrehumbert 1991; Shepherd et al. 2000). During tracer redistribution, distinct structures of high or low concentration may arise around attracting or repelling kinematical skeletons known as Lagrangian coherent structures (LCSs; Haller and Yuan 2000; Shadden et al. 2005). Recent studies in regional domains show that the mathematical framework of mixing offers promising tools to identify atmospheric circulation features associated with precipitation and moisture transport (Garaboa-Paz et al. 2015, 2017;

Corresponding author: Gabriel M. P. Perez, gabrielmpp@protonmail.com

Niang et al. 2020; Perez et al. 2021). However, there are still no global climatologies to support more general discussions and conclusions about the relationships between mixing and precipitation.

In this study, we address two main questions: 1) Can we employ the framework of mixing and LCSs to objectively identify converge zones and other structures relevant for regional precipitation regimes, expanding the results of Perez et al. (2021) to a global domain? 2) What is the nature and spatiotemporal scales of the mixing–precipitation relationship? To answer these questions, we present a 30-yr global climatology of mixing and LCSs in reanalysis data and discuss the spatial distribution and temporal variability of precipitation in light of this climatology. We investigate interannual, seasonal, and subseasonal scales of variability, focusing on the role of general circulation features such as subtropical anticyclones and monsoons in providing a favorable environment for the formation of moisture bands and precipitation.

2. Methods and data

a. Mixing diagnostics: FTLE and LCSs

To diagnose mixing in the horizontal atmospheric flow, we first obtain a two-dimensional flow from the scaling of the vertically integrated moisture flux by the total column water vapor [$\mathbf{V}_{\rho_v}$; Eq. (1)]. The aim of weighting the horizontal momentum $\mathbf{V}_H$ by the water vapor content ρ_v on each level is to construct a horizontal flow that is representative of levels along which the moisture transport is stronger. This 2D flow is more appropriate to investigate moisture pathways than simply taking a pressure level close to the surface such as 925 or 850 hPa, which could overlap with topography. Alternatively, a more computationally expensive three-dimensional trajectory integration could be performed. However, the two-dimensional $\mathbf{V}_{\rho_v}$ is useful to diagnose the horizontal features of moisture accumulation (Garaboa-Paz et al. 2015; Perez et al. 2021).

$$\mathbf{V}_{\rho_v} = \frac{\int_0^\infty \rho_v \mathbf{V}_H dz}{\int_0^\infty \rho_v dz} \quad (\mathrm{m\ s}^{-1}). \qquad (1)$$

The flow $\mathbf{V}_{\rho_v}$ is then spatially smoothed such that only its large-scale components are retained. This is done by calculating the spherical harmonics of the wind field and retaining wavenumbers smaller than 20 (Sardeshmukh and Hoskins 1984). This spatial smoothing is not expected to significantly affect the position of LCSs, since displacement errors of Lagrangian features are at least 6 times smaller than the resolution of the wind field (Methven and Hoskins 1999). The procedure substitutes the smoothed spherical spline interpolation employed in Perez et al. (2021) as it allows a more explicit control on the spatial scales that are retained.

In time-dependent flows, coherent tracer filaments are expected to emerge due to a process known as chaotic mixing (Aref 1984; Ottino 1989; Lapeyre 2002; Balasuriya et al. 2018; Ghosh et al. 2021). The kinematical skeletons underlying

these filaments are referred to as LCSs (Haller and Yuan 2000; Shadden et al. 2005). One way to characterize mixing and identify attracting LCSs in $\mathbf{V}_{\rho_v}(t)$ is to compute the backward finite-time Lyapunov exponent (FTLE) in sliding finite time windows $\Delta t = t_1 - t_0$ with $t_1 > t_0$. The FTLE [$\sigma(x_0)$, Eq. (2)] measures the average stretching rate experienced by back-trajectories departing from the neighborhood of x_0 after being advected in the two-dimensional wind field $\mathbf{V}_{\rho_v}(t)$ for a time interval Δt. The time interval chosen here was 2 days, as this is long enough to allow trajectories to explore large-scale weather systems, but it is well within the median residence time of moisture in the atmosphere of 4 days (Läderach and Sodemann 2016):

$$\sigma(\mathbf{x}_0) = \frac{1}{|\Delta t|} \ln[\sqrt{\lambda_{\max}(C)}], \qquad (2)$$

where $\lambda_{\max}$ is the largest eigenvalue of the Cauchy–Green strain tensor (C). Attracting LCSs can be found as ridges of the FTLE. Here we employ a relaxed version of the ridge criteria proposed by Shadden et al. (2005) that seeks for curves that are parallel to FTLE contours and normal to the direction of most negative FTLE curvature. Shadden et al. (2005) argue that such ridges approximate transport barriers, with small perpendicular flux. A more detailed description of the trajectory computation, ridge detection and linear algebra routines can be found in Perez et al. (2021) and are available online (see their "Code availability" section).

Figure 1 exemplifies the methodology for a particular day in the ERA5 dataset. Figures 1a and 1b represent the locations of departure, or origin points, of trajectories that arrived at each grid box. The departure points were found after two days of back-propagation in $\mathbf{V}_{\rho_v}$. Figure 1c shows the FTLE and the associated LCSs, computed based on the departure points in Figs. 1a and 1b. Trajectories of air with similar arrival points can originate from a wide range of longitudes (Fig. 1a) and latitudes (Fig. 1b). In regions of strong mixing, there are particularly sharp gradients of origin latitude and longitude, revealing interfaces of air masses. Parcels arriving in regions of sharp gradients are associated with strong stretching in the back-trajectory integration, as revealed by the FTLE ridges (LCSs) in Fig. 1c. A visual interpretation of parcel stretching around LCSs can be found in Haller (2015). In fact, Cohen and Kreitzberg (1997) employed FTLE ridges to identify airstream boundaries around extratropical cyclones in the North Atlantic.

Figure 2 illustrates two examples of the evolution of TCWV and precipitation around LCSs identified at the same timestamp (Fig. 2a) and 48 h after (Fig. 2b) the timestamp of Fig. 1 (15 December 1989). The example in Fig. 2a shows a filament of high TCWV aligned with a set of LCSs around a cyclone close to the coast of Europe; precipitation contours closer to the cyclone core also align with the same set of LCSs. After 2 days, in Fig. 2c, a second cyclone arises close to northeastern North America. Around this second cyclone, we notice a new set of LCSs whereby contours of high FTLE and precipitation are aligned. The second example, in Figs. 2b and 2d, shows that contours of precipitation and high TCWV
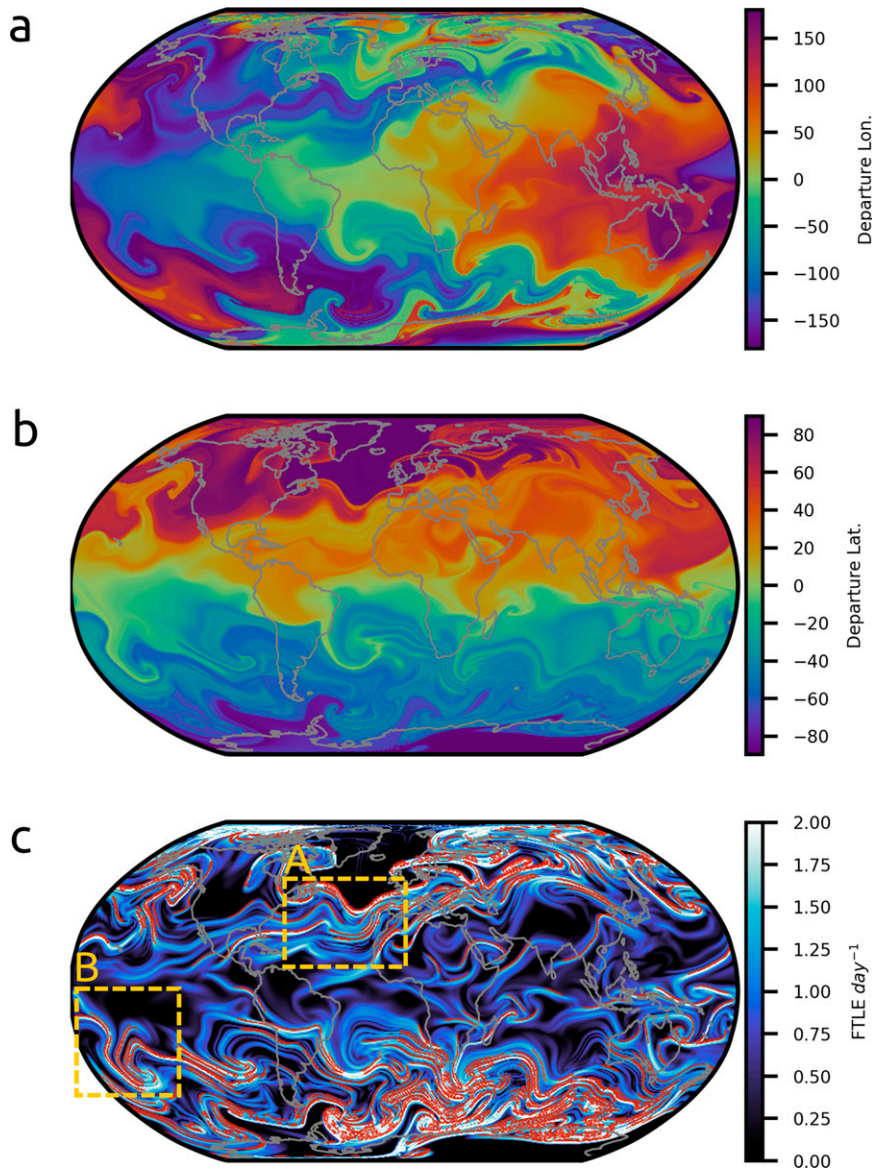
FIG. 1. Diagnostics of large-scale mixing on $\mathbf{V}_{\rho_v}$ on 15 Dec 1989 using ERA5 data. (a),(b) The departure longitudes and latitudes, respectively, of parcels arriving in a regular 0.5° lat–lon grid after 2 days of backward advection. (c) Blue shading indicates the FTLE while LCSs are depicted as red filaments. Regions A and B shown in (c) are the spatial domains for the case studies in Fig. 2.

in the South Pacific evolve to become aligned with the LCSs. Both examples illustrate how LCSs resulting from synoptic-scale mixing in $\mathbf{V}_{\rho_v}$ reshape TCWV and precipitation. Such case studies can be combined with the ones in Garaboa-Paz et al. (2015) and Perez et al. (2021) to build the hypothesis that precipitation and synoptic-scale mixing features are related in different regions across the globe.

b. Precipitation and mixing covariability

The examples in Fig. 2 reveal moisture and precipitation bands aligned along LCSs. This is expected due to the role of mixing in shaping gradients of tracers in fluid flows (Ottino 1989; Lapeyre 2002). Recalling that the FTLE was computed in a horizontal and spatially filtered flow [$\mathbf{V}_{\rho_v}$; Eq. (1)] based on the 2-day back-trajectories, we are characterizing horizontal mixing in the synoptic scale. In tropical regions, a synoptic-scale enhancement of column moisture has been observed to start two days before precipitation events (Holloway and Neelin 2010). In the extratropics, where parcel saturation typically only happens via adiabatic cooling, horizontal moisture transport may still play a role in determining the intensity of precipitation events, such as when filaments of high TCWV are created by Rossby wave breaking (de Vries 2021).
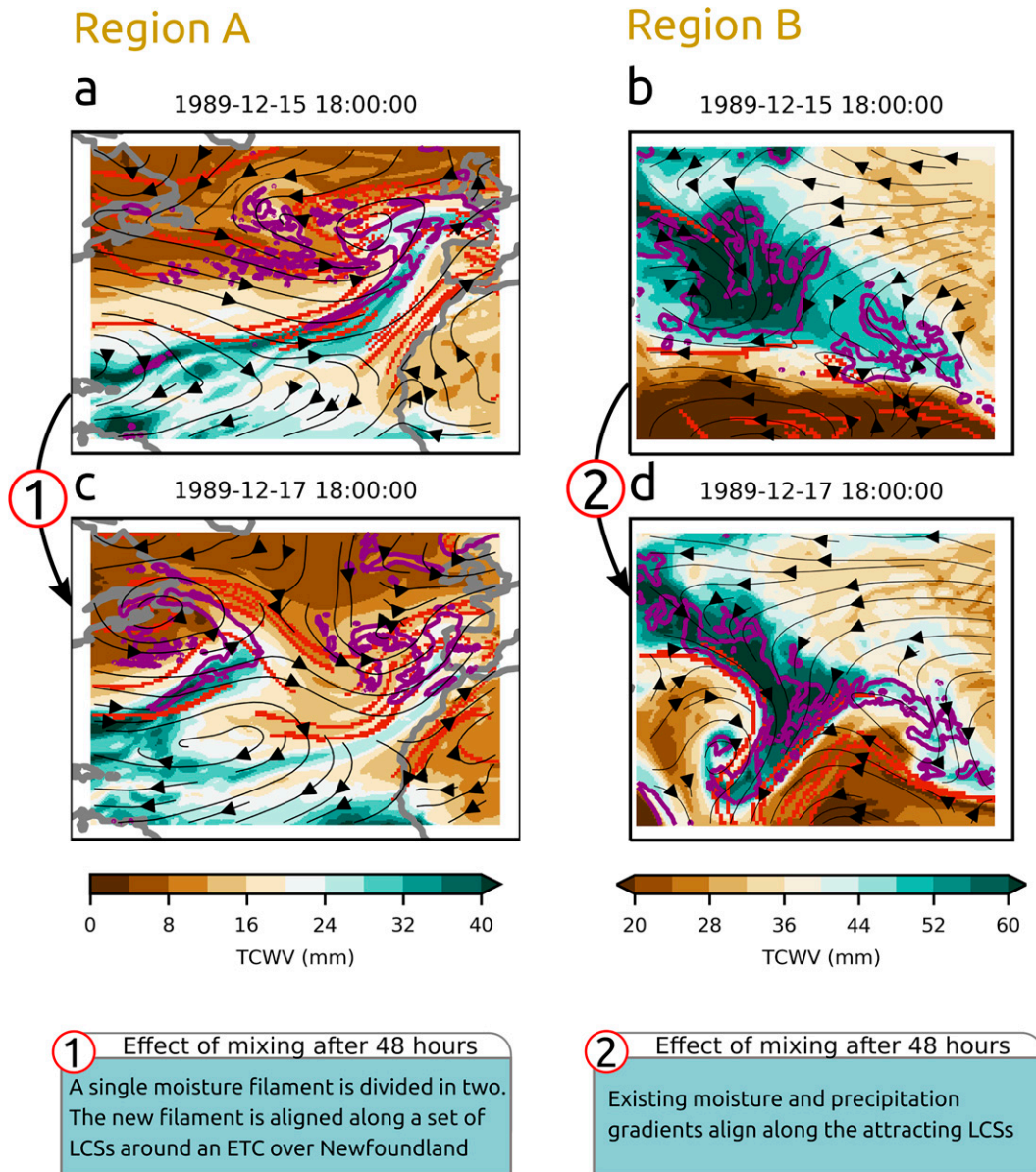
Region A

Region B

① Effect of mixing after 48 hours
A single moisture filament is divided in two. The new filament is aligned along a set of LCSs around an ETC over Newfoundland

② Effect of mixing after 48 hours
Existing moisture and precipitation gradients align along the attracting LCSs

FIG. 2. Examples of the interaction between total column water vapor (TCWV), precipitation (purple contours denote rates above 2 mm day^{-1}), and LCSs (red filaments) over the (a),(c) North Atlantic and (b),(d) South Pacific. The spatial domains of regions A and B are depicted in Fig. 1c.

To assess if this relationship that takes place in synoptic time scales reflects on longer time scales, we compute the monthly averages of the FTLE and precipitation and identify their principal modes of covariability through the partial least squares (PLS) decomposition. By performing the covariability analysis on monthly means, we substantially reduce the computational cost of the PLS decomposition at the expense of potentially obscuring the interpretation of causal relationships between mixing and precipitation. The covariability analysis on monthly means, however, still reveals important circulation mechanisms associated with precipitation anomalies, as shown in the results section

(section 3), and in section 4c we expand the discussion on possible causal pathways.

The PLS finds R pairs of latent variables $\boldsymbol{\xi}_r$, $\boldsymbol{\omega}_r$, with r in $\{1, 2, \ldots, R\}$, that maximize the information retained from $\mathbf{X}^T\mathbf{Y}$ in the least squares sense, where $\mathbf{X}$ and $\mathbf{Y}$ correspond to two-dimensional arrays of FTLE and precipitation with latitude–longitude dimensions stacked as columns and time as rows. A description of the PLS algorithm can be found in Wegelin (2000); the author also provides an interesting discussion on how the PLS algorithm relate with canonical correlation analysis.

Considering the uneven area of grid boxes in a regular latitude–longitude grid, before applying the PLS method, we

multiply $\mathbf{X}$ and $\mathbf{Y}$ by a weight vector $\mathbf{w}$ that is a function of the latitude vector $\boldsymbol{\theta}$: $\mathbf{w} = \sqrt{\cos(\boldsymbol{\theta})}$. This a standard approach to scale climate data before employing methods based on quadratic covariance matrices (Chung and Nigam 1999; Hawkins and Sutton 2007).

The first pair of latent variables $(\boldsymbol{\xi}_1, \boldsymbol{\omega}_1)$ is obtained by finding coefficient vectors $\mathbf{u}_1$ and $\mathbf{v}_1$ that maximize

$$\text{Cov}(\boldsymbol{\xi}_1, \boldsymbol{\omega}_1) = \text{Cov}(\mathbf{X}\mathbf{u}_1, \mathbf{Y}\mathbf{v}_1). \tag{3}$$

Each subsequent pair of latent scores $(\boldsymbol{\xi}_r, \boldsymbol{\omega}_r)$ is computed by repeating the procedure on the residual matrices $[\mathbf{X}^{(r)}, \mathbf{Y}^{(r)}]$ obtained by subtracting approximations based on the existing pairs of scores $\{(\boldsymbol{\xi}_1, \boldsymbol{\omega}_1) \dots (\boldsymbol{\xi}_r, \boldsymbol{\omega}_r)\}$ from the original matrices $(\mathbf{X}, \mathbf{Y})$.

In the case of atmospheric data, $\mathbf{u}_r$ and $\mathbf{v}_r$ correspond to the spatial patterns, or modes, that map the pair of latent variables $(\boldsymbol{\xi}_r, \boldsymbol{\omega}_r)$ to the original $\mathbf{X}$ and $\mathbf{Y}$ matrices. After reversing the latitude weighting, these spatial modes are physically interpretable: they are proportional to the covariance between the original variable $\mathbf{X}$ or $\mathbf{Y}$ and the latent variable of the other ($\mathbf{Y}$ or $\mathbf{X}$). Therefore, the spatial modes are presented in the appendix as correlations between one variable (FTLE or precipitation) of each grid point and the latent variable of the other.

By construction, the pairs of latent variables (ξ_1, ω_1) are maximally correlated; this correlation is close to 1 in the case of the first four modes presented in the section 3. Therefore, for each of the four pairs of modes, we have chosen to discuss only one element of the pair (i.e., the latent scores associated with the FTLE). By taking this viewpoint, we are implicitly addressing this question: What are the FTLE modes that best explain the precipitation variability? The time series of the precipitation scores are presented in the appendix.

3. Results

In this section we present global climatologies and seasonal anomalies of the FTLE and LCS occurrence; these are compared with global climatologies and seasonal anomalies of precipitation and simple diagnostics of general circulation features. All the data employed in this study originate from the ECMWF's ERA5 comprising the period between 1980 and 2009. We start with a description of the spatiotemporal variability of large-scale mixing and examine where this variability could be linked with mechanisms of coherent precipitation (e.g., ITCZ) using monthly averaged FTLE, LCS occurrence, and precipitation data. We then focus on subseasonal scales and analyze FTLE and LCS composites using daily averaged data to investigate mechanisms underpinning changes of precipitation associated with modes of variability such as the Madden–Julian oscillation (MJO) and the North Atlantic Oscillation (NAO), narrowing the analysis to the Atlantic–Americas sector. Finally, we present meridional overturning anomalies to explain an observed influence of the NAO on South American/South Atlantic precipitation.

a. Global climatology of large-scale mixing and LCSs

Here we describe general aspects of the global climatologies of mixing, LCSs, and precipitation (Fig. 3) grouped by latitudinal [section 3a(1)] and longitudinal [section 3a(2)] sectors.

1) MERIDIONAL VARIABILITY

(i) Extratropical features

In the extratropics, we first notice that LCS frequency of occurrence peaks at the midlatitudes while the FTLE peaks at higher latitudes. We can compare regions north and south of the stars in Figs. 3a and 3b. The higher mixing in high latitudes can be explained by the parcel deformation caused by the increased ETC core activity in those regions (Jones and Simmonds 1993; Ulbrich et al. 2009). Cyclone cores, however, are characterized as elliptic LCSs (Haller and Beron-Vera 2012; Haller 2015), while the LCSs identified here as FTLE ridges are expected to identify hyperbolic material lines (Haller 2002); hence the lower frequency of occurrence of LCSs in higher latitudes in Fig. 3b. Fronts, on the other hand, can be identified as FTLE ridges (Cohen and Kreitzberg 1997; Garaboa-Paz et al. 2015) and are more frequent at the midlatitudes (Berry et al. 2011). Therefore, the discrepancies between FTLE intensity and LCS frequency of occurrence in the extratropics can be understood in terms of the spatial distribution of ETC cores and fronts.

(ii) Subtropical features

In some subtropical regions such as South America, southern North America, the South Pacific, and East Asia, diagonal FTLE contours and high LCS occurrence (denoted by squares in Figs. 3a,b) coincide with precipitation features (Fig. 3c); examples include the South Atlantic convergence zone (SACZ) region at 15°S, 45°W; the mei-yu front region at 20°N, 140°E; the south Indian convergence zone region at 20°S, 45°E; and North America around Mexico and the southern United States (23°N, 105°W). These regions are known to be under strong precipitation seasonality driven by convergence zones (Kodama 1992) and monsoon systems (Rodwell and Hoskins 2001); these systems will be further discussed in section 3b. We also note that these subtropical FTLE/LCS maxima are typically positioned in between subtropical anticyclones.

(iii) Equatorial features

High FTLE and LCS occurrence bands are collocated with the typical position of the ITCZ (triangles in Figs. 3a,b). Particularly in the Atlantic and east Pacific, these bands are located between the northern and southern subtropical gyres, revealing the approximation of trajectories associated with the encounter of the southeasterlies and northeasterlies. This suggests that the interface between semi-stationary eddies produces strong deformation. The strong FTLE values (Fig. 3a) and frequent occurrence of LCSs (Fig. 3b) along the ITCZ suggest that the development of organized precipitation bands
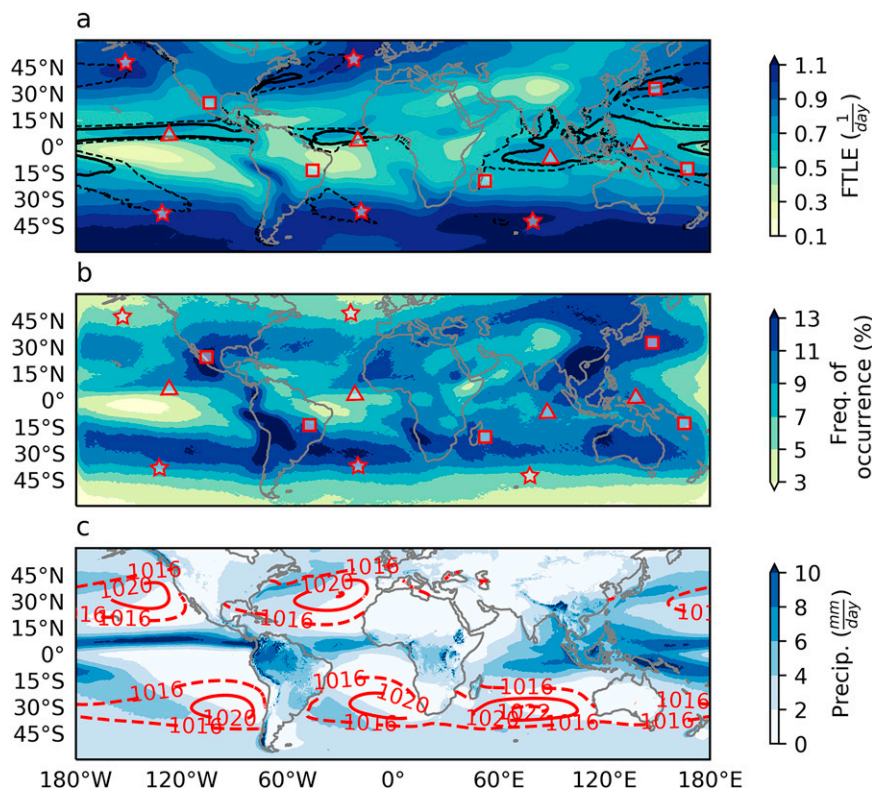
FIG. 3. Averages between 1980 and 2009 of (a) FTLE (filled contours) and 4 and 6 mm day^{-1} precipitation contours (dashed and solid black contours, respectively), (b) frequency of LCS occurrence over a homogeneous area of ~3100 km^2, and (c) precipitation and mean sea level pressure. Red polygons in (a) and (b) are there to assist the text.

is favored by the large-scale flow kinematics, potentially driving precipitation in those regions.

2) ZONAL VARIABILITY

(i) The Atlantic and east Pacific

The large-scale mixing pattern characterized by the FTLE and LCS occurrence (Fig. 3) in the Atlantic (70°W–15°E) is similar to that of the east Pacific (180°–90°E). Both sectors present 1) high precipitation and FTLE features in the ITCZ region, 2) mixing minima on the equatorward flank of the subtropical highs, and 3) mixing and precipitation maxima along the poleward flanks of the subtropical highs. The similar relative positions of the subtropical anticyclones (Fig. 3c) and the presence of subtropical convergence zones in South America and South Pacific are possible explanations for the likeness between the Atlantic/east Pacific regimes of precipitation and mixing.

(ii) The west Pacific

In the west Pacific sector (120°W–180°), in contrast to the Atlantic and the east Pacific, there are no equatorial FTLE and LCS occurrence maxima (Figs. 3a,b). This is expected, considering that the absence of subtropical anticyclones in the west Pacific (Fig. 3c) reduces the meridional shear of the

zonal winds, consequently reducing the deformation of trajectories at the equatorial band. There is, however, a strong signature of ITCZ precipitation in that region (Fig. 3c), suggesting that, in this region, the ITCZ is driven mainly by local thermodynamics rather than by the horizontal redistribution of moisture by the large-scale flow; this is consistent with the dominance of convective precipitation over stratiform precipitation in the west Pacific (Berg et al. 2002). In the Maritime Continent, high contours of FTLE and LCSs overlap with heavy precipitation around the western Pacific warm pool and the SPCZ. In Northeast Asia, this collocation of high mixing and precipitation contour occurs around the typical location of the mei-yu front and ETC fronts.

(iii) Africa and the Indian Ocean

In the southern part of the African continent there are distinct mixing and LCS features, such as the Congo air boundary and the Kalahari discontinuity; the latter, located at the southwest African coast, presents a particularly strong signature in Fig. 3b. These southern African features are known as "drylines" and represent boundaries between moist and dry air (Howard and Washington 2019). In the Indian Ocean sector, the main tropical LCS and FTLE feature is a maximum at about 15°N stretching from East Africa to the Indian
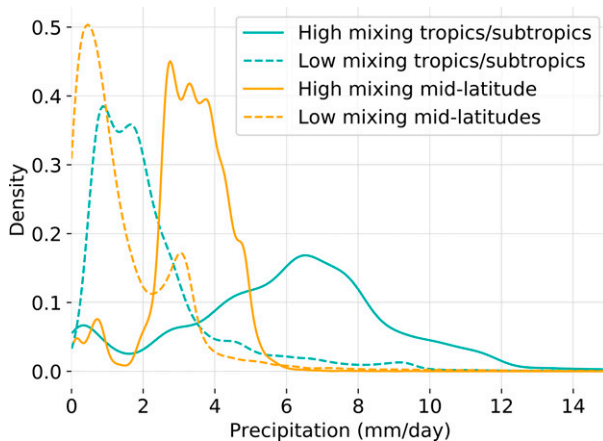
FIG. 4. Probability density functions of the mean daily precipitation grid boxes in Fig. 3c separated by latitudinal band and degree of mixing. Subtropical latitudes are defined between 20°N and 20°S and midlatitudes are defined between 20° and 50°N/S. High and low mixing points are separated based on the FTLE value of the grid box using quantiles of 0.1 for low mixing and 0.9 for high mixing. The quantiles are calculated as a function of latitude.

peninsula collocated with the position of the Somali jet. Near the island of Madagascar at about 18°S, high FTLE, LCS, and precipitation contours coincide around the typical position of the south Indian convergence zone (SICZ; Cook 2000).

Figure 4 summarizes the spatial relationship between the averages of mixing and precipitation by showing the probability density functions (PDFs) of the mean daily precipitation grid boxes divided by (i) intensity of mixing and (ii) latitudinal band. High and low mixing grid boxes are defined above and below FTLE quantiles of 0.9 and 0.1. The quantiles are computed as a function of latitude, so that points reveal distinct mixing regions in relation to their latitudinal band. Tropical and subtropical regions are selected between 20°S and 20°N and midlatitudes are defined as 20°–50°S and 20°–50°N. We notice that separating precipitation by mixing categories produces clearly distinct precipitation PDFs for both the tropics/ subtropics and the midlatitudes. In the midlatitudes, the shape of the precipitation PDFs in high and low mixing regions remains similar, but it is shifted toward higher values in the high mixing case. In the tropics and the subtropics, the precipitation PDF in high mixing regions presents both a higher median and higher standard deviation than the precipitation PDF in low mixing regions.

In this section, the spatial analysis of FTLE and precipitation features reveals that, in many regions of the globe, high FTLE and LCS occurrence is collocated with regions of high precipitation. Many of these locations have been identified in literature as regions of convergence zones using a variety of metrics. Our results indicate the usefulness of the proposed framework as a unified diagnostic for identifying convergence zones. In the next section, we present an account of the spatiotemporal variability of the precipitation–FTLE relationship.

b. Interannual and seasonal mixing–precipitation relationship

When comparing the precipitation PDFs in Fig. 4, there is a clear distinction between the grid boxes of low and high mixing. However, since the FTLE is measuring the Lagrangian strain within a time interval of 2 days, its association with precipitation is not expected to be necessarily local in space (i.e., at the gridbox level); instead, this association is expected to comprise a neighborhood around the FTLE feature [see discussion in Perez et al. (2021)].

The PLS method is employed here to embed monthly averaged FTLE and precipitation data into pairs of latent variables that are maximally correlated; these latent variables model the covariance relationships between mixing and precipitation considering the entire spatial domain. To reduce the computational cost of the PLS method as well as remove high-frequency signals, the datasets are downsampled to the monthly scale by calculating the monthly averages of the 6-hourly precipitation and FTLE. The PLS algorithm processes the monthly datasets to produce four pairs of FTLE– precipitation latent variables that are most strongly correlated; the time series of the latent modes are shown in the appendix (Fig. A2).

Figure 5 shows the monthly average (solid lines) and the interannual variability (shading) of the FTLE modes embedded by the PLS method. We notice that the first mode is strongly seasonal; its amplitude peaks around December–February (DJF) and June–August (JJA). Mode 2 also varies seasonally, but with smaller amplitude than mode 1 and peaking in the transition seasons. Mode 3 also presents a clear seasonality, but peaks twice a year in May and November. The interannual variability of the first three modes, represented by the shading, is smaller than their intra-annual variability. Mode 4, on the other hand, varies more strongly at the interannual scale.

The first four FTLE modes identified by the PLS decomposition retain a substantial part of the precipitation variance, particularly over the continent in equatorial and subtropical regions (Fig. 6) and over the ocean around the ITCZ. In these regions, the explained variance typically over 50% and as high as 90% indicates that the monthly precipitation is well explained by the FTLE modes, pointing to a strong temporal relationship between the two variables. Figure 6b shows, for comparison, the explained variance of a linear regression fitted to explain the precipitation time series in each grid box using the associated FTLE time series of the same grid box. In some tropical and subtropical regions, the fraction of the variance explained by the PLS algorithm is similar to the grid box linear regression. In these regions, the temporal FTLE– precipitation relationship is local in space. However, in other locations, such as the Sahel and storm track regions, the PLS explained variance is much higher than the grid box regression, suggesting that remote mixing features may be influencing precipitation in those regions.

Considering the substantial FTLE-mixing covariability shown in Fig. 6, in the next sections we discuss specific time scales of this covariability, starting from longer (interannual)
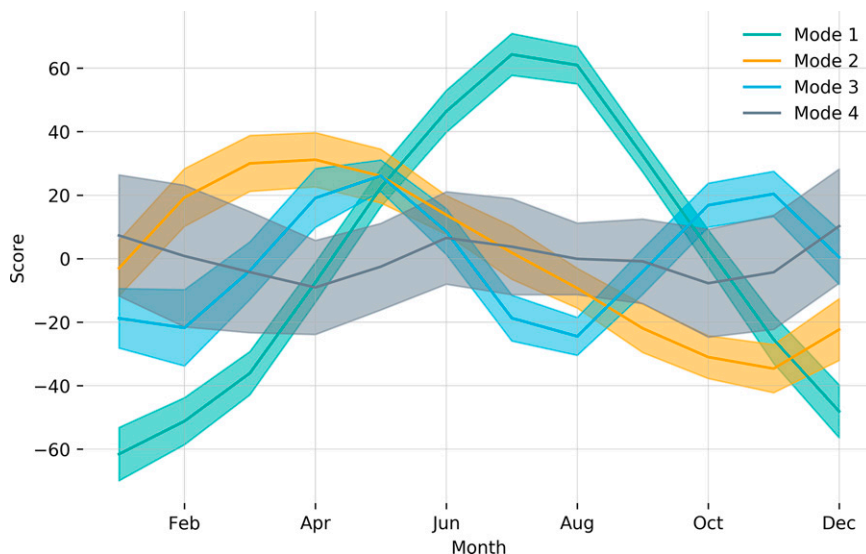
Fig. 5. Monthly means of the PLS scores (latent variables) associated with modes 1–4. The shaded areas represent the interannual standard deviation.

to shorter time scales (seasonal and subseasonal). We focus the discussion on the tropical and subtropical regions where the precipitation variability is better explained both by the PLS modes and by the gridbox linear regression.

1) Interannual variability–ENSO

The fourth FTLE mode presents a strong interannual variability. An obvious candidate to be driving this mode is El Niño–Southern Oscillation (ENSO), an atmospheric–oceanic coupled mechanism (Jin 1997) known to directly drive tropical precipitation through changes in the Walker circulation (Ambrizzi et al. 2004) and influence precipitation regimes at higher latitudes through teleconnection mechanisms (Grimm and Silva Dias 1995; Sulca and Rocha 2021). The atmospheric component of the ENSO is typically quantified by the Southern Oscillation index (SOI), a standardized sea level pressure difference between Tahiti and Darwin, Australia.

Figure 7 shows time series of the SOI monthly average along with the scores of the fourth FTLE mode obtained by the PLS method. Simple visual inspection shows that the two
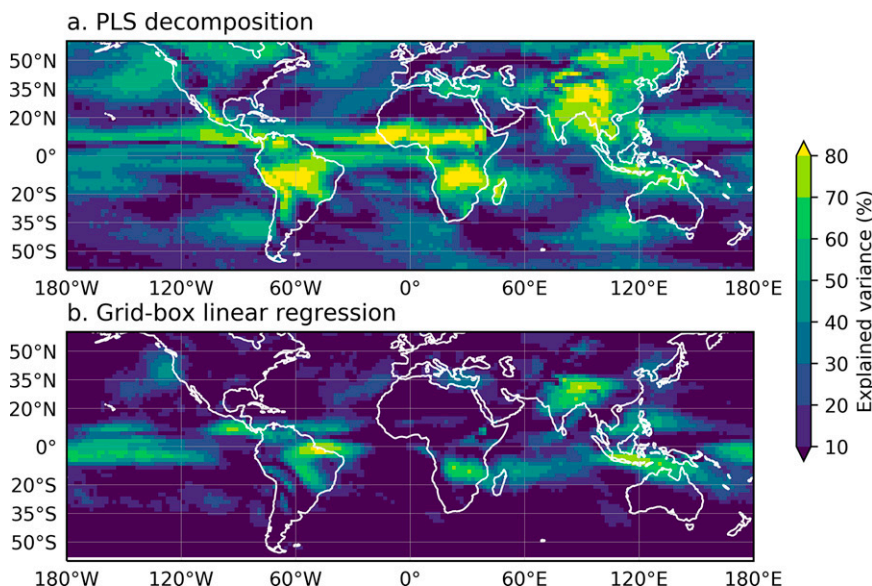

Fig. 6. Fraction of the precipitation variance (Pearson's r^2) explained by (a) the four FTLE latent variables obtained by the PLS decomposition and (b) a linear regression of the associated gridpoint FTLE and precipitation time series.
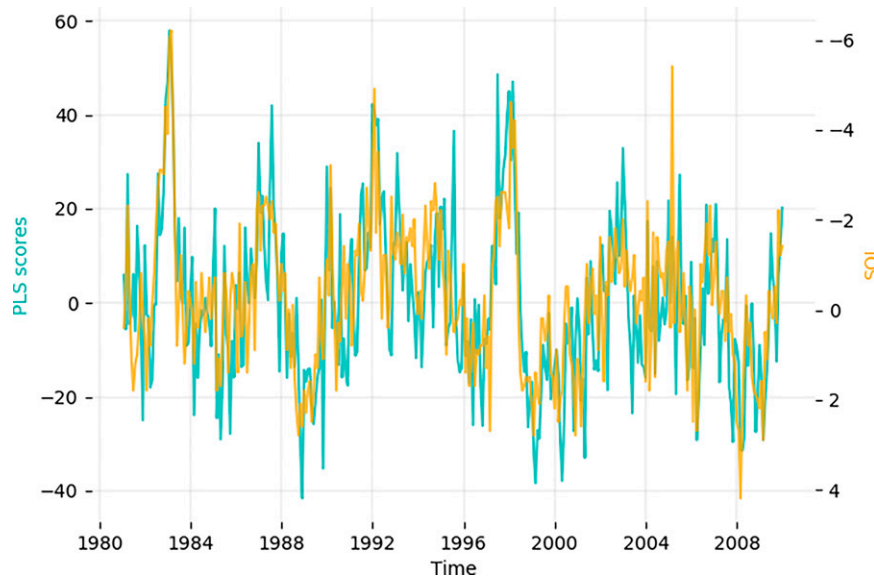
FIG. 7. Scores associated with mode 4 of the PLS method (left axis) and the Southern Oscillation index (SOI; right axis).

time series are well correlated. This indicates that ENSO drives[1] this fourth FTLE mode and, more broadly, underpins the precipitation–mixing relationship on interannual scales.

Figure 8 shows the FTLE and precipitation anomalies in months of positive (El Niño) and negative (La Niña) ENSO events defined based on the Niño-3.4 index, a measure of sea surface temperature anomaly in the central Pacific that is commonly used to define such events. The FTLE and precipitation anomalies were calculated in relation to the total temporal mean (i.e., the fields shown in Figs. 3a,c). In the equatorial Pacific, there is a collocation between FTLE and precipitation anomalies, indicating a direct impact of the transition of the Walker cell on mixing and precipitation in this region. Remote effects of ENSO on precipitation can be seen in many parts of the world. In many of these remote regions, such as South America and southern Africa, precipitation anomalies are collocated with FTLE anomalies of the same sign. Thus, during ENSO events, higher than average FTLE leads to anomalously high monthly precipitation totals and vice versa.

2) SEASONAL VARIABILITY

Considering that the first PLS mode characterizes the DJF–JJA variation (Fig. 5), it is of interest to investigate links between precipitation and mixing during these seasons. Figure 9 shows FTLE and precipitation anomalies along with MSLP in DJF and JJA. The anomalies were calculated by taking the seasonal average and subtracting from the total average (i.e., the fields shown in Figs. 3a,c). We employed the MSLP as a diagnostic of general circulation features, namely the subtropical

anticyclones associated with the descending branch of the Hadley overturning circulation.

Figure 9 shows anomalies of precipitation and FTLE in DJF and JJA. In most tropical and subtropical regions, these anomalies are of the same sign and visually similar. In particular, the winter/summer migration of the ITCZ precipitation seems to be accompanied by a migration of positive FTLE anomalies. The FTLE anomalies along the equator seem vary according to the strength of the MSLP centers of the adjacent subtropical highs in the Atlantic and east Pacific, suggesting that equatorial mixing is associated with the subtropical anticyclones. On the other hand, the seasonal migration of equatorial mixing in the Indian ocean can be described in terms of the Southeast Asia monsoon winds and the south Indian subtropical high. These migrations will be described in the following paragraphs.

(i) Atlantic

The South Atlantic subtropical high presents a strong seasonality (Fig. 9), a feature that is particularly influenced by precipitation in the South American monsoon (Rodwell and Hoskins 2001; Reboita et al. 2019). In DJF, equatorial FTLE and precipitation positive anomalies are displaced south as the South Atlantic high pressure center weakens. In JJA, the South Atlantic high is substantially stronger and the positive FTLE anomalies migrate north at about 10°N. The North Atlantic high is also stronger in JJA, although its seasonality is less pronounced. This suggests that, at the equator, the 2-day FTLE characterizes the deformation along the interface of adjacent anticyclones. The migration of this interface (indicated by positive equatorial FTLE anomalies) is in close agreement with the zonal migration of equatorial precipitation, suggesting that the seasonal migration of the Atlantic ITCZ could be linked with the ability of the large-scale horizontal flow to organize moisture filaments. In other words,

---

[1] The causal inference here is simply based on the assumption that ENSO can be explained independently of atmospheric mixing or precipitation patterns.
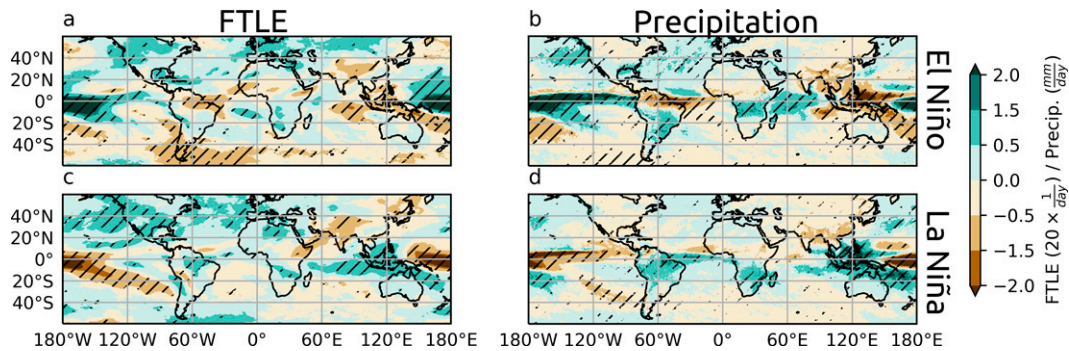
FIG. 8. (a),(c) FTLE and (b),(d) mean precipitation anomalies during (a),(b) El Niño and (c),(d) La Niña events. Hatched anomalies are significant at the 1% level based on a Student's *t* test for the null hypothesis that the mean of El Niño and La Niña events are not different from total temporal mean.

Fig. 9 suggests that the migration of the Atlantic ITCZ is linked to the migration of the band of maximum FTLE. The strength of this band of maximum FTLE appears to be associated with the strength of the adjacent anticyclones.

(ii) Pacific

We notice a similar behavior in the eastern Pacific in terms of the relationship between the strength of subtropical gyres and mixing–precipitation at the equator. The North Pacific high is substantially stronger in JJA and the FTLE and precipitation anomalies are positive at 10°N. In DJF, the FTLE and precipitation anomalies at 10°N become negative as the North Pacific high weakens. This suggests that, in the east Pacific, mixing and precipitation along the ITCZ are also linked with the strength of the adjacent subtropical anticyclones. In the western Pacific, we notice a close agreement between FTLE and precipitation anomalies around the Maritime Continent and northern Australia.

(iii) Africa and the Indian Ocean

In DJF, FTLE (Fig. 9a) and precipitation (Fig. 9b) positive anomalies stretch from Madagascar to the Maritime Continent. DJF is the dry season of the Indian monsoon, during

which the low-level flow is expected to come from the Asian continent to the Indian Ocean. This suggests that the stronger mixing over the Indian Ocean in DJF is characterized by the Lagrangian deformation at the interface between the southeasterlies from the South Indian subtropical high and the outflow from the Asian monsoon. During JJA, the Asian monsoon wet phase, the Lagrangian deformation over the tropical Indian Ocean is expected to decrease, as the monsoon winds will not be in opposition to the southeasterlies from the subtropical anticyclone. Accordingly, in JJA, both the FTLE (Fig. 9c) and precipitation (Fig. 9d) anomalies are negative over the tropical Indian Ocean.

c. Intraseasonal variability in the Atlantic and South America

In the previous section we employed the PLS method and composite analyses to show that precipitation and mixing are related on seasonal and interannual scales in various regions around the globe. Here, we narrow down our analysis to the east Pacific, Americas, and Atlantic sectors to investigate the mixing–precipitation relationship under specific modes of subseasonal variability, namely the Madden–Julian oscillation and the North Atlantic Oscillation. This section focuses on
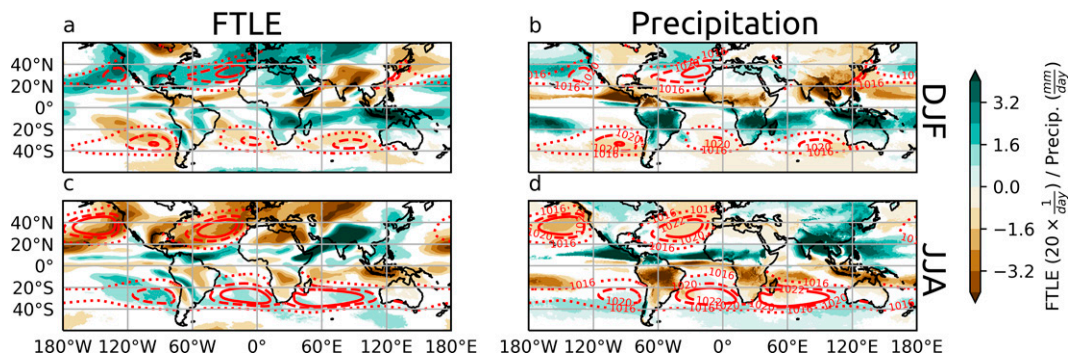

FIG. 9. Seasonal anomalies of (a),(c) FTLE and (b),(d) precipitation in (a),(b) DJF and (c),(d) JJA. Average mean sea level pressure is shown in red contours for each season. Precipitation and FTLE contours are only shown when significant at the 1% level based on a Student's *t* test for the null hypothesis that the mean of each season is not different from the total temporal mean.

the DJF season, the season in which MJO peaks are stronger and the winter NAO is well defined. Global maps of the results presented here can be found in the appendix.

1) MJO

In phases 8 and 1, the MJO transitions from a slow and wet Kelvin–Rossby wave to a fast and dry Kelvin wave while it propagates eastward across the east Pacific and Atlantic. Before entering the dry Kelvin wave regime, MJO pulses trigger Rossby wave trains that enhance precipitation in the SACZ and the SPCZ; it elongates the SPCZ precipitation eastward (Matthews 2012) and enhances the SACZ (Grimm 2019). In phases 4 and 5, the effect of the MJO teleconnection is opposite; precipitation is suppressed in the SACZ and SPCZ regions. In the other phases (2, 3, 6, and 7) the FTLE, LCS occurrence, and precipitation anomalies are consistently weaker.

Figure 10 shows anomalies of the FTLE, precipitation, and LCS occurrence during MJO pulses in DJF. MJO events are defined when the amplitude of the real-time multivariate MJO index (RMM; Wheeler and Hendon 2004) is greater than one. The anomalies are computed as the difference between the averages during MJO events of each phase and the seasonal mean of DJF. In many cases, there is an agreement in the signs of FTLE, LCS, and precipitation anomalies. In phases 1 and 8, the frequency of LCSs, the FTLE, and precipitation anomalies are enhanced over South America and South Pacific. In phases 4 and 5, this behavior is opposite: the large-scale mixing is less favorable for moisture filamentation in the SACZ and SPCZ regions, as indicated by negative FTLE and LCS anomalies coinciding with negative precipitation contours. However, there are cases where FTLE and LCS anomalies are not reflected as precipitation anomalies, such as in northwestern Amazon during phase 1.

2) NAO

The equatorial Atlantic has a strong influence on South American precipitation because the meridional gradient of Atlantic equatorial sea surface temperatures (SSTs) and the position of the Atlantic ITCZ modulate spatial and temporal variability of precipitation over northeastern Brazil and the Amazon (Souza and Cavalcanti 2009; Yoon and Zeng 2010; Marengo et al. 2011; Jones and Carvalho 2018). On the other hand, the tropical Atlantic SSTs are modulated by the strength of the surface easterlies in the subtropical North Atlantic, where the effect of North Atlantic Oscillation is strong (Hurrell et al. 2003; Kushnir et al. 2006; Souza and Cavalcanti 2009). This suggests that the NAO could influence precipitation over South America on subseasonal time scales, but the extent of these teleconnections has not been quantified in the literature.

This section investigates whether there is any influence of the NAO on South American precipitation at subseasonal scales in DJF, focusing on the role of mixing structures in this interhemispheric teleconnection, as an example of the potential use of these mixing diagnostics to disentangle mechanisms of precipitation variability.
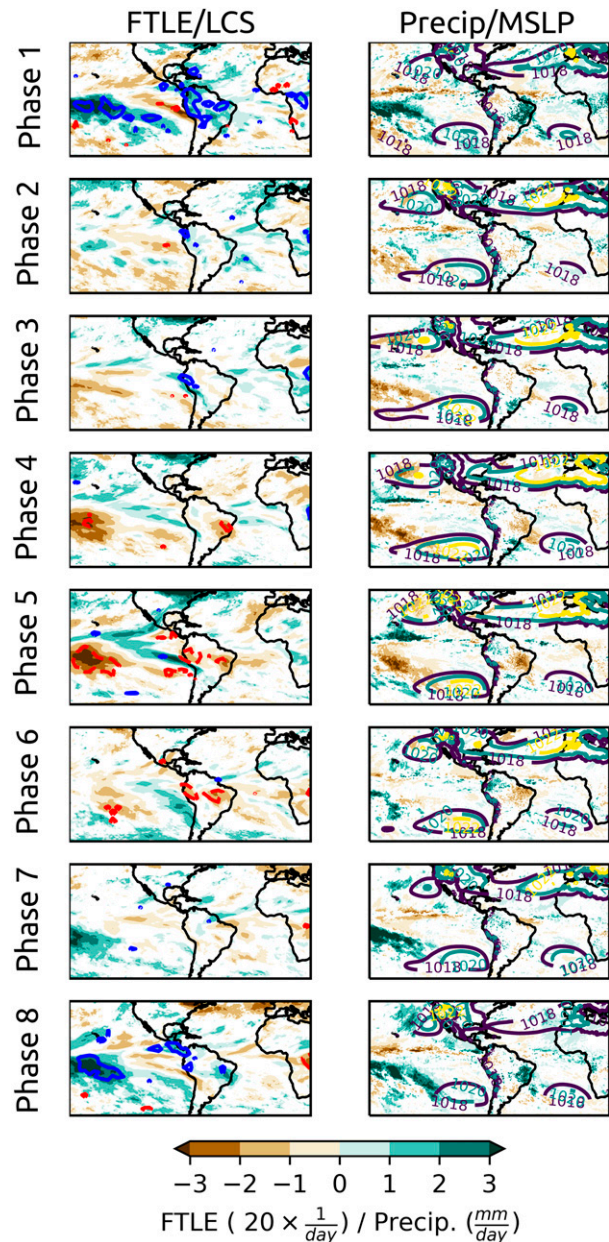

FIG. 10. Anomalies during MJO events in DJF of (left) FTLE and LCS occurrence and (right) precipitation. LCS frequency of occurrence anomalies in the left column are shown as red and blue contours, representing anomaly levels of −2% and +2%, respectively. MSLP contours are also shown in the right column. Precipitation and FTLE contours are only shown when significant at the 1% level based on a Student's t test for the null hypothesis that the MJO events have the same mean of the season (DJF).

Events associated with the positive and negative phases of the NAO (Hurrell et al. 2003) are defined first by computing the normalized time series of the first empirical orthogonal function (EOF) of the MSLP field over the Atlantic sector (20°–80°N, 90°W–40°E) using ERA5 data. Subsequently, a positive NAO event is defined when the index is higher than 1

for at least 6 consecutive days, with at least a 20-day separation from the latest previously defined event. Negative NAO events are defined in an analogous fashion, but with a negative threshold for the first principal component time series index. Figure A3 in the appendix illustrates the selection of events.

We now focus on the differences between positive and negative NAO pulses in DJF (hereafter referred to as NAO anomalies). The anomalies were temporally smoothed in a 5-day window centered around each lag. The lagged NAO precipitation composites in Figs. 11d and 11f show significant anomalies 5 and 10 days after the pulse around the ITCZ and the South American continent. Interestingly, the associated FTLE and LCS occurrence anomalies in Figs. 11c and 11e indicate that large-scale flow kinematics is unfavorable for the formation of moisture bands, hence suppressing the formation of coherent precipitation features such as the SACZ. Considering that these anomalies are composed by the difference between positive and negative NAO events, Fig. 11 tell us that positive NAO events suppress the SACZ and enhance the ITCZ, while negative NAO events have the opposite effect. The anticyclonic anomalies of $\mathbf{V}_{\rho_v}$ in Fig. 11d in the South Atlantic suggest that the negative FTLE anomalies at the SACZ region may be explained by an intensification of the South Atlantic subtropical high.

Figure 11 suggests an interhemispheric teleconnection, where NAO pulses propagate to the Southern Hemisphere, controlling mixing and precipitation in South America. We hypothesize that there is a causal relationship linking NAO pulses and South American precipitation mediated by the Hadley meridional overturning. This hypothesis can be described as follows: positive (negative) NAO pulses strengthen (weaken) the upwelling at the ITCZ, strengthening (weakening) the southern Hadley cell and the downwelling at the South Atlantic anticyclone (notice the anticyclonic anomalies at lag +10 days in Fig. 11).

To support this hypothesis, Fig. 12 shows the anomalies of vertical wind speed zonally averaged between 75° and 20°W. Similarly to Fig. 11, the anomalies are shown as differences between positive and negative NAO events and averaged in 5-day windows around each lag. On the day of the NAO pulse (lag 0), the strongest anomalies are in the Northern Hemisphere, where descending motion is enhanced between 30°–60°N. Five days after the event, weaker vertical motion anomalies appear around the middle and upper tropospheric levels (200–600 hPa) in subtropical latitudes (0°–30°N). Ten days after the event's peak, the dominating anomalies are in the Southern Hemisphere. The enhanced downwelling around 25°S is consistent with the anticyclonic anomalies at lag +10 days in Fig. 11, which indicates a strengthening of the South Atlantic high.

Together, Figs. 11 and 12 suggest that NAO pulses propagate via the Hadley overturning, establishing vertical wind speed anomalies in the Southern Hemisphere. These anomalies seem to modulate the large-scale horizontal flow around the South Atlantic anticyclone, thus controlling mixing and the occurrence of LCSs at the SACZ and ITCZ regions. Changes in frequency and intensity of these convergence

zones then contribute to the precipitation anomalies observed in South America after the NAO pulse. An alternative hypothesis to explain the anomalies in Fig. 11 is offered in the next section.

4. Discussion

a. Spatial distribution of mixing and LCSs

Broadly speaking, the horizontal distribution of the 2-day FTLE (Fig. 3a) indicates that high values of horizontal mixing are related to the typical positions or interfaces of semipermanent and transient eddies such as ETCs and subtropical anticyclones. Regions of minimal mixing can be seen along the equatorward branches of subtropical gyres, indicating that trajectories behave as parallel southeasterly or northeasterly flows. Along the ITCZ, higher mixing is indicated between these northern and southern easterlies. At the poleward edges of the subtropical gyres, FTLE maxima suggest that the interaction between the anticyclones and ETCs produce a highly mixed environment; this is noticeable mainly at the North Atlantic and North Pacific. This is consistent with numerical experiments performed by Lapeyre (2002) in idealized 2D turbulence; the authors point out that regions whereby eddies interact are associated with higher FTLE values.

The LCS frequency of occurrence in Fig. 3b naturally bears some similarities with the FTLE distribution, considering that LCSs are defined as FTLE ridges. However, while the average intensity of mixing increases with latitude [this is also shown by Garaboa-Paz et al. (2017)], the frequency of occurrence of LCSs decreases rapidly at latitudes higher than 45°. This is consistent with the frequency of occurrence of ETC fronts, which typically peaks at midlatitudes and decreases closer to the pole (Catto et al. 2014). Other aspects, however, could explain the high-latitude FTLE–LCS comparative discrepancy. For example, it could be that the internal dynamics of some ETCs is such that they do not fall within our definition of LCSs in $\mathbf{V}_{\rho_v}$. From another point of view, it could also be the case that some aspects of the ETCs are more appropriately defined as other types of coherent structures, such as hyperbolic or elliptic LCSs (Serra et al. 2017). Regardless, a case-study oriented investigation could help uncover the relationship between ETCs and LCSs.

b. Precipitation–mixing association

The FTLE and precipitation are associated at multiple spatial and temporal scales. Global averages of FTLE and precipitation spatially collocated; regions of stronger mixing are associated with higher precipitation medians and more frequent extremes (Fig. 4). This FTLE–precipitation relationship is not only spatial, but spatiotemporal, as shown by the PLS decomposition and seasonal/interannual composites—that is, FTLE and precipitation anomalies are not only collocated, but their temporal variability is in phase in many regions.

The interannual PLS mode is highly correlated with the SOI index, indicating that the ENSO modulates the global FTLE–precipitation covariability (Fig. 7). Moreover, significant FTLE and precipitation anomalies are collocated during
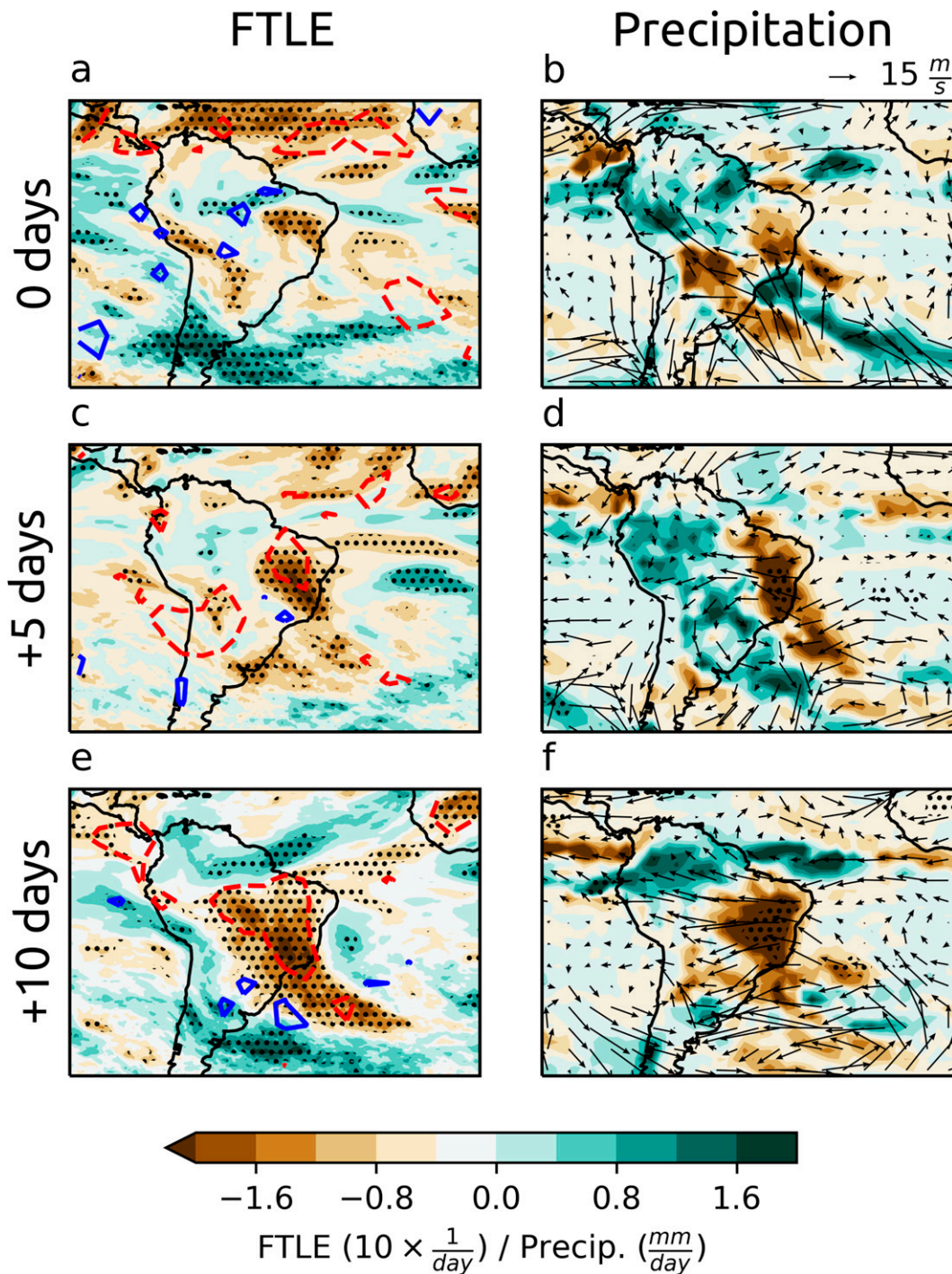
FIG. 11. Lagged anomalies of FTLE, LCS frequency of occurrence, precipitation, and $\mathbf{V}_{\rho_v}$ during NAO events in DJF. (left) FTLE anomalies in filled contours and LCS occurrence in blue and red contours, representing anomaly levels of −2% and +2%, respectively. (right) Precipitation and $\mathbf{V}_{\rho_v}$ anomalies. Stippled anomalies are significant at the 1% level based on a Student's t test for the null hypothesis that positive and negative NAO events have the same mean.

El Niño and La Niña months (Fig. 8). This suggests that some of the remote ENSO precipitation anomalies are associated with changes of large-scale mixing that may favor or suppress the development of organized moisture bands depending on

the phase of the oscillation. In southern Africa, for example, coherent cloud bands associated with the SICZ are more likely to happen during La Niña events (Hart et al. 2018); consistently, there are significant positive FTLE anomalies during
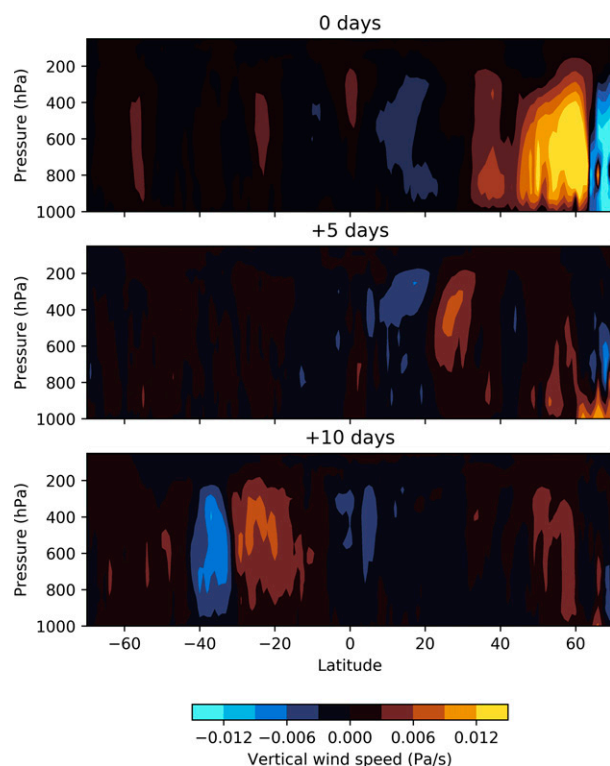
FIG. 12. Vertical wind speed difference (Pa s^{-1}) between positive and negative NAO events in DJF averaged in a longitudinal slice over the Atlantic and Americas (75°–20°W).

La Niña events in that region (Fig. 8d). In South America, the precipitation dipole that reverses sign depending on the ENSO phase (Bombardi et al. 2014) can be explained by FTLE anomalies. These FTLE anomalies suggest that the impacts of ENSO on South American precipitation are mediated by the ITCZ and the SACZ, considering that the FTLE is a diagnostic for both convergence zones (Perez et al. 2021).

At the seasonal scale, the dominant PLS mode peaks in JJA and DJF, suggesting that precipitation and mixing variability are connected through summer and winter mechanisms such as the migration of the Hadley cell. This is further confirmed by the seasonal anomalies of precipitation, FTLE, and MSLP in Fig. 9, where we see that tropical and subtropical anomalies of precipitation and FTLE are collocated, particularly along the ITCZ and monsoon regions. We notice that the sign and intensity of the FTLE anomalies near the Atlantic and Pacific ITCZ are associated with the strength of the adjacent subtropical anticyclones (i.e., in JJA mixing is stronger at the ITCZ while the MSLP of the anticyclones is also stronger). The opposite happens in DJF. This suggests a direct link between the Hadley overturning and horizontal large-scale mixing at the tropics. Rodwell and Hoskins (2001) discussed the role of tropical precipitation in idealized simulations in producing realistic subtropical anticyclones.

At subseasonal scales, the FTLE composites highlight important mechanisms of precipitation. During MJO pulses in

DJF, precipitation, mixing, and LCS occurrence anomalies in the Pacific, the Americas, and the Atlantic are collocated. This supports that the MJO controls precipitation in those regions by the means of enhancing or suppressing kinematical mechanisms like convergence zones. The agreement between the FTLE and precipitation anomalies is especially noticeable in southeastern and northeastern Brazil during phases 1 and 8, where the propagation of Rossby waves through the Pacific–South Atlantic channel has been shown to enhance SACZ precipitation (Grimm 2019). Noticeably, in the Atlantic ITCZ, around the northeastern coast of South America, the FTLE does not seem to explain the negative precipitation anomalies in phase 1. In that phase, the fast Kelvin wave is known to suppress precipitation in that region (Sobel and Kim 2012). The absence of a counterpart negative FTLE anomaly indicates that this precipitation suppression does not rely on the horizontal kinematics of moisture transport. Interestingly, Rossby waves, such as the MJO teleconnection through the PSA channel, seem to be more effective in creating the FTLE anomalies than equatorial Kelvin waves. Shepherd et al. (2000) observed the same effect when comparing mixing regimes in the stratosphere and the mesosphere: the stratospheric flow, dominated by Rossby waves, is more likely to generate coherent tracer filaments than the mesospheric flow, typically dominated by high wavenumbers.

Similarly to the MJO, the NAO lagged composites (Fig. 11) also indicate the existence of a remote influence on precipitation by the means of changing the horizontal kinematics of moisture distribution: after an NAO pulse, significant precipitation anomalies arise around the ITCZ and SACZ regions; these anomalies are collocated with FTLE anomalies. In Fig. 12, we explore the hypothesis that this teleconnection is mediated by the Atlantic Hadley overturning (Fig. 12). An alternative, but not mutually exclusive, hypothesis would be that the MJO acts as a confounding factor, controlling both the NAO and the South American precipitation. We notice that the negative FTLE and precipitation anomalies in South America after NAO pulses (Fig. 11) are similar to the MJO anomalies in phases 4 and 5 (Fig. 10). Indeed, the MJO modulates the impact of the NAO consistently: in phases 4 and 5, the MJO intensifies positive NAO pulses while suppressing negative NAO pulses (Cassou 2008). Considering that the MJO acts as a confounding factor, a more detailed investigation should be performed before establishing a firm causal link between the NAO and South American precipitation.

c. A comment on mixing–precipitation causal pathways

Broadly speaking, the results suggest a causal relationship between features of large-scale horizontal mixing and precipitation. A possible causal pathway is that large-scale mixing features reshape the moisture distribution, controlling regional precipitation regimes. This causal pathway is based on the following: 1) the flow $\mathbf{V}_{\rho_v}$ [Eq. (1)] was defined to represent the moisture pathways, 2) ridges of the backward FTLE [Eq. (2)] represent attracting structures, and 3) the back-trajectories were computed well within the median residence time of moisture in the atmosphere. The causal relationship
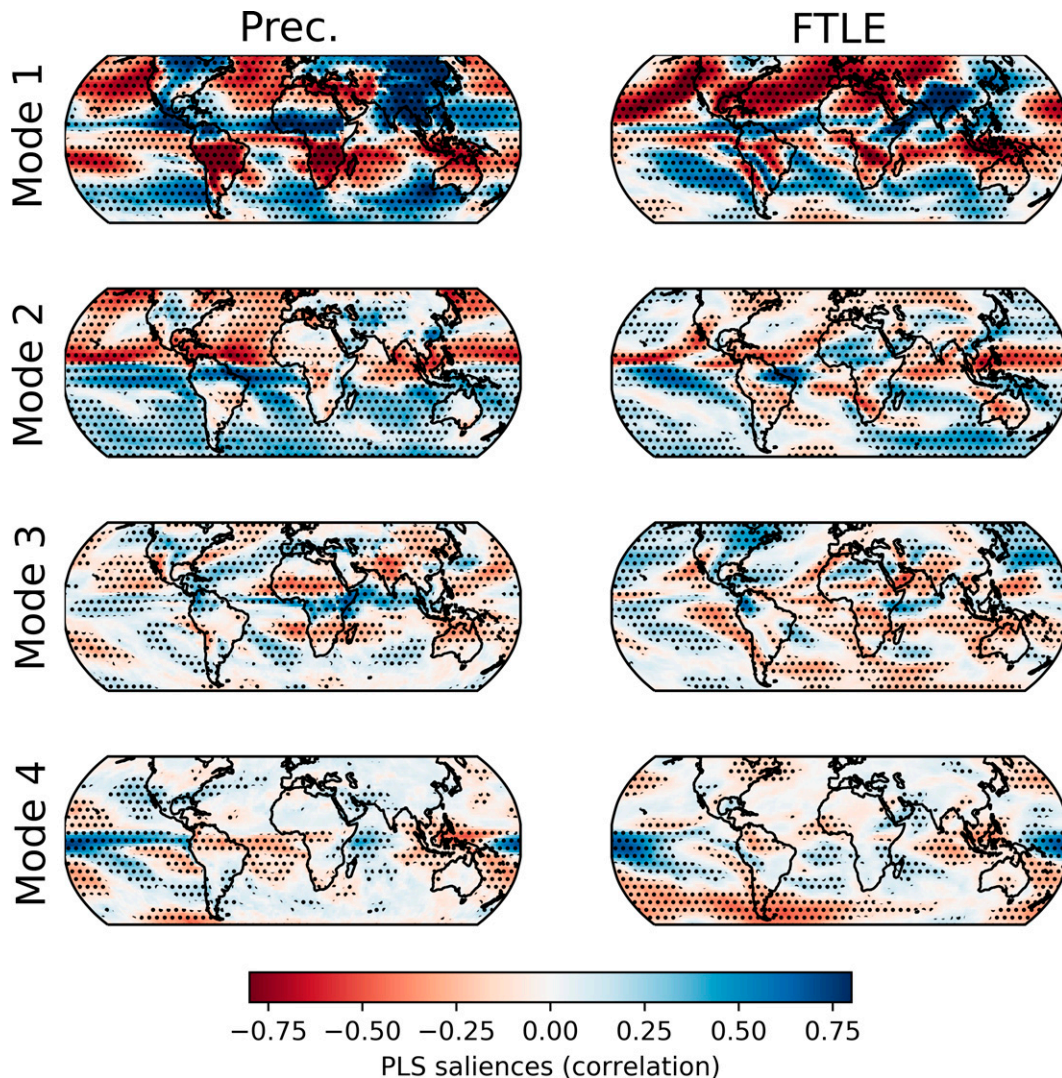
FIG. A1. (left) Precipitation and (right) FTLE spatial modes obtained from the PLS decomposition. Stippling shows correlations significant at the 1% level based on a Student's *t* test.

could also go in the opposite direction (i.e., precipitation features may cause changes in horizontal mixing). For example, the condensational heating associated with precipitating clouds intensifies the low-level horizontal shear and dilation of air parcels (Dias and Pauluis 2009), potentially influencing the FTLE. Such codependence between mixing and precipitation could even create a positive feedback mechanisms. For example, near the Atlantic and Pacific ITCZ in JJA, the band of positive FTLE anomalies (Fig. 9) favors the organization of coherent cloud bands that increase precipitation, which, in turn, might increase existing positive FTLE anomalies.

Alternatively, it could be argued that the FTLE–precipitation relationship is not one of cause and effect. In other words, the purely kinematic ability of the flow to shape the horizontal moisture distribution has little or no influence on precipitation and vice versa. This could be the case when mixing features coincide with dynamically active regions (i.e., regions of intense vertical motion) with enough local moisture supply such that large-scale transport does not contribute significantly to precipitation. However, this is unlikely to be the case in most regions since the median residence time of moisture even in dynamically active structures such as ETCs (estimated to be approximately 2 days; Papritz et al. 2021) is long enough for moisture trajectories to be deformed by the large-scale flow. Nonetheless, this potential confounding effect could be untangled in a future study by decomposing precipitation anomalies in terms of vertical motion and moisture anomalies. Such decomposition would quantify the individual contributions of kinematics (horizontal transport) and dynamics to precipitation.

5. Conclusions and final remarks

In this study we present a global climatology of the finite-time Lyapunov exponent (FTLE) and Lagrangian coherent
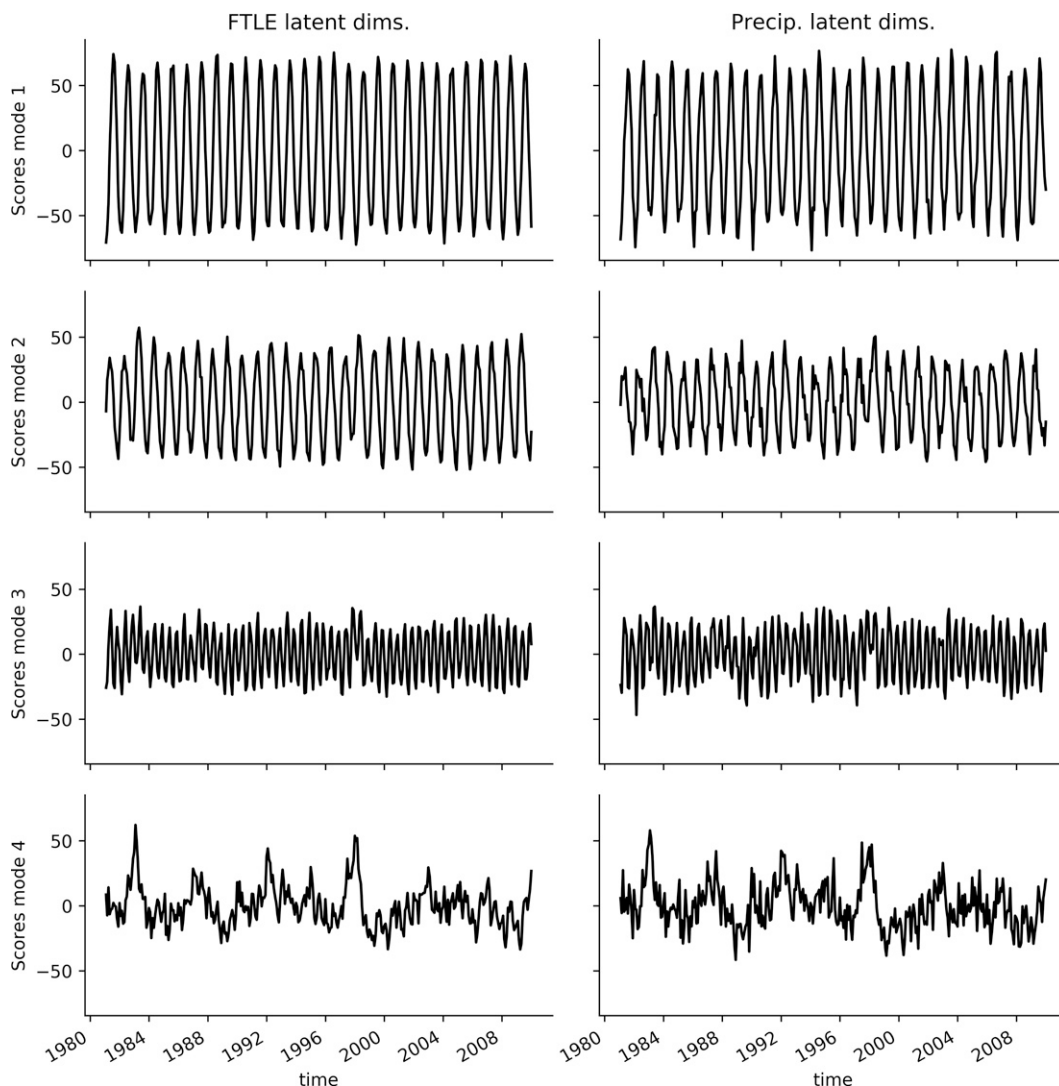
FIG. A2. Time series of the four pairs of latent variables obtained from the PLS decomposition.

structures (LCSs), discussing the relationship between mixing and precipitation features on subseasonal, seasonal, and interannual scales. We show that a number of aspects of precipitation variability can be explained by mixing features, particularly in tropical and subtropical regions. These results extend the analyses of Perez et al. (2021) to a global scale, suggesting that attracting LCSs are able to identify convergence zones and other similar precipitation mechanisms without relying on region-specific information such as existing convergence zone detection algorithms.

The application of the conceptual and mathematical framework of mixing and LCSs is in still its early stages in meteorology and remains unknown to the majority of field experts. This is unsurprising, considering that the theoretical basis is relatively recent (Haller and Yuan 2000) and still undergoing development (Balasuriya et al. 2018; Nolan et al. 2020). Moreover, the computation of Lagrangian diagnostics is usually

more complex and expensive than Eulerian diagnostics, with little literature on how to overcome the practical limitations of processing global atmospheric data. However, we argue that there is much to be gained by the weather and climate communities from adopting Lagrangian kinematic frameworks, especially if we consider that the concentration of long-lived properties directly impacts human activities—examples include volcanic ash (Dacre and Harvey 2018), biomass-burning smoke (Gonzalez-Alonso et al. 2019), and water vapor. In the context of climate change, identifying the underlying mechanisms of moisture accumulation and their relationships with precipitation can help assess the limitations of climate models in the present climate and derive storylines to provide useful information for decision-makers where changes in regional precipitation regimes are uncertain (Shepherd 2014).

We hope that the broad nature of the analyses presented here will motivate future studies in the use of Lagrangian
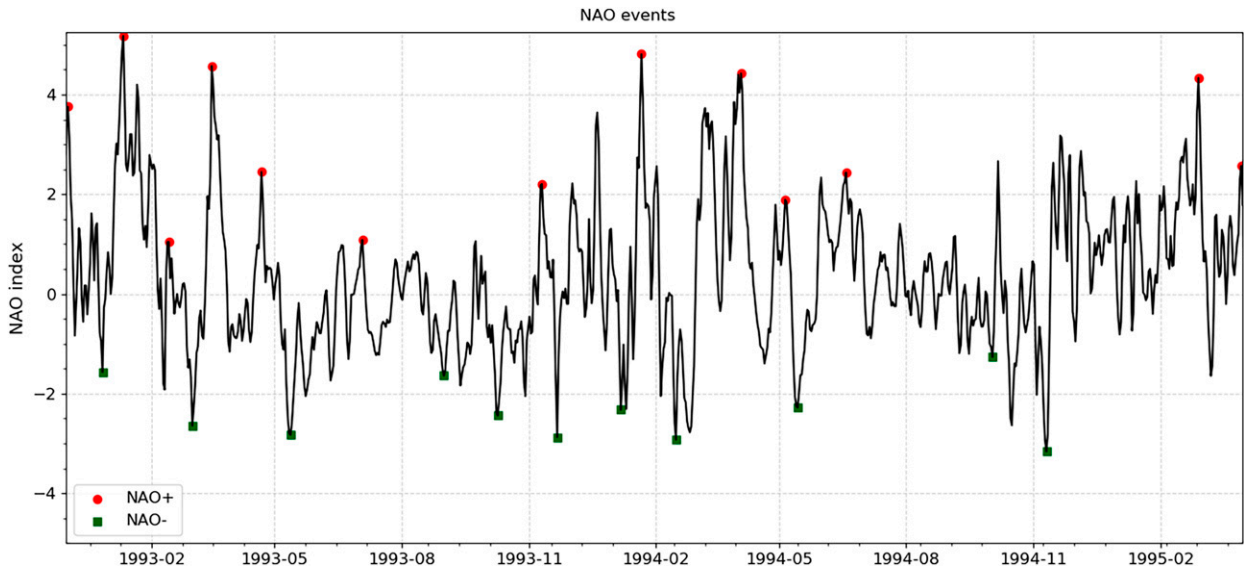
FIG. A3. Time series of the normalized first principal component of the Atlantic sector sea level pressure, referred to as the NAO index. NAO positive events are marked with a red circle and negative events with a green square.

kinematics to diagnose features associated with coherent tracer accumulation, such as tropical rainbands and fronts.

APPENDIX

Supporting Figures

Figures A1 and A2 show, respectively, the spatial modes and the time series of scores of the PLS decomposition. Figure A3 shows the time series of the NAO index to illustrate the identification of positive and negative NAO events.

REFERENCES

Ambrizzi, T., E. B. de Souza, and R. S. Pulwarty, 2004: The Hadley and Walker regional circulations and associated ENSO impacts on South American seasonal rainfall. *The Hadley Circulation: Present, Past and Future*, Springer, 203–235.

Aref, H., 1984: Stirring by chaotic advection. *J. Fluid Mech.*, **143**, 1–21, https://doi.org/10.1017/S0022112084001233.

Balasuriya, S., N. T. Ouellette, and I. I. Rypina, 2018: Generalized Lagrangian coherent structures. *Physica D*, **372**, 31–51, https://doi.org/10.1016/j.physd.2018.01.011.

Berg, W., C. Kummerow, and C. A. Morales, 2002: Differences between east and west Pacific rainfall systems. *J. Climate*, **15**, 3659–3672, https://doi.org/10.1175/1520-0442(2002)015<3659:DBEAWP>2.0.CO;2.

Berry, G., and M. J. Reeder, 2014: Objective identification of the intertropical convergence zone: Climatology and trends from the ERA-Interim. *J. Climate*, **27**, 1894–1909, https://doi.org/10.1175/JCLI-D-13-00339.1.

——, ——, and C. Jakob, 2011: A global climatology of atmospheric fronts. *Geophys. Res. Lett.*, **38**, L04809, https://doi.org/10.1029/2010GL046451.

Bombardi, R. J., L. M. Carvalho, C. Jones, and M. S. Reboita, 2014: Precipitation over eastern South America and the South Atlantic sea surface temperature during neutral ENSO periods. *Climate Dyn.*, **42**, 1553–1568, https://doi.org/10.1007/s00382-013-1832-7.

Cassou, C., 2008: Intraseasonal interaction between the Madden–Julian oscillation and the North Atlantic oscillation. *Nature*, **455**, 523–527, https://doi.org/10.1038/nature07286.

Catto, J. L., N. Nicholls, C. Jakob, and K. L. Shelton, 2014: Atmospheric fronts in current and future climates. *Geophys. Res. Lett.*, **41**, 7642–7650, https://doi.org/10.1002/2014GL061943.

Chung, C., and S. Nigam, 1999: Weighting of geophysical data in principal component analysis. *J. Geophys. Res.*, **104**, 16 925–16 928, https://doi.org/10.1029/1999JD900234.

Cohen, R. A., and C. W. Kreitzberg, 1997: Airstream boundaries in numerical weather simulations. *Mon. Wea. Rev.*, **125**, 168–183, https://doi.org/10.1175/1520-0493(1997)125<0168:ABINWS>2.0.CO;2.

Cook, K. H., 2000: The south Indian convergence zone and interannual rainfall variability over southern Africa. *J. Climate*, **13**, 3789–3804, https://doi.org/10.1175/1520-0442(2000)013<3789:TSICZA>2.0.CO;2.

Dacre, H. F., and N. J. Harvey, 2018: Characterizing the atmospheric conditions leading to large error growth in volcanic ash cloud forecasts. *J. Appl. Meteor. Climatol.*, **57**, 1011–1019, https://doi.org/10.1175/JAMC-D-17-0298.1.

——, P. A. Clark, O. Martinez-Alvarado, M. A. Stringer, and D. A. Lavers, 2015: How do atmospheric rivers form? *Bull. Amer. Meteor. Soc.*, **96**, 1243–1255, https://doi.org/10.1175/BAMS-D-14-00031.1.

de Vries, A. J., 2021: A global climatological perspective on the importance of Rossby wave breaking and intense moisture transport for extreme precipitation events. *Wea. Climate Dyn.*, **2**, 129–161, https://doi.org/10.5194/wcd-2-129-2021.

Dias, J., and O. Pauluis, 2009: Convectively coupled waves propagating along an equatorial ITCZ. *J. Atmos. Sci.*, **66**, 2237–2255, https://doi.org/10.1175/2009JAS3020.1.

Garaboa-Paz, D., J. Eiras-Barca, F. Huhn, and V. Pérez-Muñuzuri, 2015: Lagrangian coherent structures along atmospheric rivers. *Chaos Interdiscip. J. Nonlinear Sci.*, **25**, 063105, https://doi.org/10.1063/1.4919768.

——, ——, and V. Pérez-Muñuzuri, 2017: Climatology of Lyapunov exponents: The link between atmospheric rivers and large-scale mixing variability. *Earth Syst. Dyn.*, **8**, 865–873, https://doi.org/10.5194/esd-8-865-2017.

Ghosh, A., K. Suara, S. W. McCue, Y. Yu, T. Soomere, and R. J. Brown, 2021: Persistency of debris accumulation in tidal estuaries using Lagrangian coherent structures. *Sci. Total Environ.*, **781**, 146808, https://doi.org/10.1016/j.scitotenv.2021.146808.

Gonzalez-Alonso, L., M. Val Martin, and R. A. Kahn, 2019: Biomass-burning smoke heights over the Amazon observed from space. *Atmos. Chem. Phys.*, **19**, 1685–1702, https://doi.org/10.5194/acp-19-1685-2019.

Grimm, A. M., 2019: Madden–Julian oscillation impacts on South American summer monsoon season: Precipitation anomalies, extreme events, teleconnections, and role in the MJO cycle. *Climate Dyn.*, **53**, 907–932, https://doi.org/10.1007/s00382-019-04622-6.

——, and P. L. Silva Dias, 1995: Analysis of tropical–extratropical interactions with influence functions of a barotropic model. *J. Atmos. Sci.*, **52**, 3538–3555, https://doi.org/10.1175/1520-0469(1995)052<3538:AOTIWI>2.0.CO;2.

Haller, G., 2002: Lagrangian coherent structures from approximate velocity data. *Phys. Fluids*, **14**, 1851–1861, https://doi.org/10.1063/1.1477449.

——, 2015: Lagrangian coherent structures. *Annu. Rev. Fluid Mech.*, **47**, 137–162, https://doi.org/10.1146/annurev-fluid-010313-141322.

——, and G. Yuan, 2000: Lagrangian coherent structures and mixing in two-dimensional turbulence. *Physica D*, **147**, 352–370, https://doi.org/10.1016/S0167-2789(00)00142-1.

——, and F. J. Beron-Vera, 2012: Geodesic theory of transport barriers in two-dimensional flows. *Physica D*, **241**, 1680–1702, https://doi.org/10.1016/j.physd.2012.06.012.

Hart, N. C., R. Washington, and C. J. Reason, 2018: On the likelihood of tropical–extratropical cloud bands in the south Indian convergence zone during ENSO events. *J. Climate*, **31**, 2797–2817, https://doi.org/10.1175/JCLI-D-17-0221.1.

Hawkins, E., and R. Sutton, 2007: Variability of the Atlantic thermohaline circulation described by three-dimensional empirical orthogonal functions. *Climate Dyn.*, **29**, 745–762, https://doi.org/10.1007/s00382-007-0263-8.

Herdies, D. L., A. da Silva, M. A. Silva Dias, and R. Nieto Ferreira, 2002: Moisture budget of the bimodal pattern of the summer circulation over South America. *J. Geophys. Res.*, **107**, 8075, https://doi.org/10.1029/2001JD000997.

Holloway, C. E., and J. D. Neelin, 2010: Temporal relations of column water vapor and tropical precipitation. *J. Atmos. Sci.*, **67**, 1091–1105, https://doi.org/10.1175/2009JAS3284.1.

Howard, E., and R. Washington, 2019: Drylines in southern Africa: Rediscovering the Congo air boundary. *J. Climate*, **32**, 8223–8242, https://doi.org/10.1175/JCLI-D-19-0437.1.

Huntley, H. S., B. Lipphardt Jr., G. Jacobs, and A. Kirwan Jr., 2015: Clusters, deformation, and dilation: Diagnostics for material accumulation regions. *J. Geophys. Res. Oceans*, **120**, 6622–6636, https://doi.org/10.1002/2015JC011036.

Hurrell, J. W., Y. Kushnir, G. Ottersen, and M. Visbeck, 2003: *An Overview of the North Atlantic Oscillation. Geophys. Monogr.*, Vol. 134, Amer. Geophys. Union, 1–35, https://doi.org/10.1029/134GM01.

Jin, F.-F., 1997: An equatorial ocean recharge paradigm for ENSO. Part I: Conceptual model. *J. Atmos. Sci.*, **54**, 811–829, https://doi.org/10.1175/1520-0469(1997)054<0811:AEORPF>2.0.CO;2.

Jones, C., and L. M. Carvalho, 2018: The influence of the Atlantic multidecadal oscillation on the eastern Andes low-level jet and precipitation in South America. *npj Climate Atmos. Sci.*, **1**, 40, https://doi.org/10.1038/s41612-018-0050-8.

Jones, D. A., and I. Simmonds, 1993: A climatology of Southern Hemisphere extratropical cyclones. *Climate Dyn.*, **9**, 131–145, https://doi.org/10.1007/BF00209750.

Kodama, Y., 1992: Large-scale common features of subtropical precipitation zones (the Baiu frontal zone, the SPCZ, and the SACZ) Part I: Characteristics of subtropical frontal zones. *J. Meteor. Soc. Japan*, **70**, 813–836, https://doi.org/10.2151/jmsj1965.70.4_813.

Kushnir, Y., W. A. Robinson, P. Chang, and A. W. Robertson, 2006: The physical basis for predicting Atlantic sector seasonal-to-interannual climate variability. *J. Climate*, **19**, 5949–5970, https://doi.org/10.1175/JCLI3943.1.

Läderach, A., and H. Sodemann, 2016: A revised picture of the atmospheric moisture residence time. *Geophys. Res. Lett.*, **43**, 924–933, https://doi.org/10.1002/2015GL067449.

Lapeyre, G., 2002: Characterization of finite-time Lyapunov exponents and vectors in two-dimensional turbulence. *Chaos*, **12**, 688–698, https://doi.org/10.1063/1.1499395.

Marengo, J. A., J. Tomasella, L. M. Alves, W. R. Soares, and D. A. Rodriguez, 2011: The drought of 2010 in the context of historical droughts in the Amazon region. *Geophys. Res. Lett.*, **38**, L12703, https://doi.org/10.1029/2011GL047436.

Matthews, A. J., 2012: A multiscale framework for the origin and variability of the South Pacific convergence zone. *Quart. J. Roy. Meteor. Soc.*, **138**, 1165–1178, https://doi.org/10.1002/qj.1870.

Methven, J., and B. Hoskins, 1999: The advection of high-resolution tracers by low-resolution winds. *J. Atmos. Sci.*, **56**, 3262–3285, https://doi.org/10.1175/1520-0469(1999)056<3262:TAOHRT>2.0.CO;2.

Niang, C., A. M. Mancho, V. J. García-Garrido, E. Mohino, B. Rodriguez-Fonseca, and J. Curbelo, 2020: Transport pathways across the West African monsoon as revealed by Lagrangian coherent structures. *Sci. Rep.*, **10**, 12543, https://doi.org/10.1038/s41598-020-69159-9.

Nolan, P. J., M. Serra, and S. D. Ross, 2020: Finite-time Lyapunov exponents in the instantaneous limit and material transport. *Nonlinear Dyn.*, **100**, 3825–3852, https://doi.org/10.1007/s11071-020-05713-4.

Ottino, J. M., 1989: *The Kinematics of Mixing: Stretching, Chaos, and Transport.* Cambridge University Press, 390 pp.

Papritz, L., F. Aemisegger, and H. Wernli, 2021: Sources and transport pathways of precipitating waters in cold-season deep North Atlantic cyclones. *J. Atmos. Sci.*, **78**, 3349–3368, https://doi.org/10.1175/JAS-D-21-0105.1.

Perez, G. M., P. L. Vidale, N. P. Klingaman, and T. Martin, 2021: Atmospheric convergence zones stemming from large-scale mixing. *Wea. Climate Dyn.*, **2**, 475–488, https://doi.org/10.5194/wcd-2-475-2021.

Pierrehumbert, R., 1991: Large-scale horizontal mixing in planetary atmospheres. *Phys. Fluids*, **3**, 1250–1260, https://doi.org/10.1063/1.858053.

Reboita, M. S., T. Ambrizzi, B. A. Silva, R. F. Pinheiro, and R. P. da Rocha, 2019: The South Atlantic subtropical anticyclone: Present and future climate. *Front. Earth Sci.*, **7**, 8, https://doi.org/10.3389/feart.2019.00008.

Rodwell, M. J., and B. J. Hoskins, 2001: Subtropical anticyclones and summer monsoons. *J. Climate*, **14**, 3192–3211, https://doi.org/10.1175/1520-0442(2001)014<3192:SAASM>2.0.CO;2.

Sardeshmukh, P. D., and B. I. Hoskins, 1984: Spatial smoothing on the sphere. *Mon. Wea. Rev.*, **112**, 2524–2529, https://doi.org/10.1175/1520-0493(1984)112<2524:SSOTS>2.0.CO;2.

Serra, M., P. Sathe, F. Beron-Vera, and G. Haller, 2017: Uncovering the edge of the polar vortex. *J. Atmos. Sci.*, **74**, 3871–3885, https://doi.org/10.1175/JAS-D-17-0052.1.

Shadden, S. C., F. Lekien, and J. E. Marsden, 2005: Definition and properties of Lagrangian coherent structures from finite-time Lyapunov exponents in two-dimensional aperiodic flows. *Physica D*, **212**, 271–304, https://doi.org/10.1016/j.physd.2005.10.007.

Shepherd, T. G., 2014: Atmospheric circulation as a source of uncertainty in climate change projections. *Nat. Geosci.*, **7**, 703–708, https://doi.org/10.1038/ngeo2253.

——, J. N. Koshyk, and K. Ngan, 2000: On the nature of large-scale mixing in the stratosphere and mesosphere. *J. Geophys. Res.*, **105**, 12433–12446, https://doi.org/10.1029/2000JD900133.

Sobel, A., and D. Kim, 2012: The MJO–Kelvin wave transition. *Geophys. Res. Lett.*, **39**, L20808, https://doi.org/10.1029/2012GL053380.

Souza, P., and I. F. A. Cavalcanti, 2009: Atmospheric centres of action associated with the Atlantic ITCZ position. *Int. J. Climatol.*, **29**, 2091–2105, https://doi.org/10.1002/joc.1823.

Sulca, J. C., and R. P. Rocha, 2021: Influence of the coupling South Atlantic convergence zone–El Niño–Southern Oscillation (SACZ-ENSO) on the projected precipitation changes over the central Andes. *Climate*, **9**, 77, https://doi.org/10.3390/cli9050077.

Ulbrich, U., G. C. Leckebusch, and J. G. Pinto, 2009: Extra-tropical cyclones in the present and future climate: A review. *Theor. Appl. Climatol.*, **96**, 117–131, https://doi.org/10.1007/s00704-008-0083-8.

Wegelin, J. A., 2000: A survey of Partial Least Squares (PLS) methods, with emphasis on the two-block case. Tech. Rep., 46 pp., https://stat.uw.edu/research/tech-reports/survey-partial-least-squares-pls-methods-emphasis-two-block-case.

Wheeler, M. C., and H. H. Hendon, 2004: An all-season real-time multivariate MJO index: Development of an index for monitoring and prediction. *Mon. Wea. Rev.*, **132**, 1917–1932, https://doi.org/10.1175/1520-0493(2004)132<1917:AARMMI>2.0.CO;2.

Wills, R. C., and T. Schneider, 2015: Stationary eddies and the zonal asymmetry of net precipitation and ocean freshwater forcing. *J. Climate*, **28**, 5115–5133, https://doi.org/10.1175/JCLI-D-14-00573.1.

Yoon, J.-H., and N. Zeng, 2010: An Atlantic influence on Amazon rainfall. *Climate Dyn.*, **34**, 249–264, https://doi.org/10.1007/s00382-009-0551-6.